ACS PHYSICAL CHEMISTRY Au
AN OPEN ACCESS JOURNAL OF THE AMERICAN CHEMICAL SOCIETY

pubs.acs.org/physchemau

Article

Na Diffusion in Hard Carbon Studied with Positive Muon Spin Rotation and Relaxation

Kazuki Ohishi,* Daisuke Igarashi, Ryoichi Tatara, Shoichiro Nishimura, Akihiro Koda, Shinichi Komaba, and Jun Sugiyama*

Cite This: ACS Phys. Chem Au 2022, 2, 98–107

Read Online

ACCESS | Metrics & More | Article Recommendations

ABSTRACT: The diffusive nature of Na^+ in Na-inserted hard carbon (C_xNa), which is the most common anode material for a Na-ion battery, was studied with a positive muon spin rotation and relaxation (μ^+SR) technique in transverse, zero, and longitudinal magnetic fields (TF, ZF, and LF) at temperatures between 50 and 375 K, where TF (LF) denotes the applied magnetic field perpendicular (parallel) to the initial muon spin polarization. At temperatures above 150 K, TF-μ^+SR measurements showed a distinct motional narrowing behavior, implying that Na^+ begins to diffuse above 150 K. The presence of two different muon sites in C_xNa was confirmed with ZF- and LF-μ^+SR measurements; one is in the Na-inserted graphene layer, and the other is in the Na-vacant graphene layer adjacent to the Na-inserted graphene layer. A systematic increase in the field fluctuation rate (ν) with increasing temperature also evidenced a thermally activated Na diffusion, particularly above 150 K. Assuming the two-dimensional diffusion of Na^+ in the graphene layers, the self-diffusion coefficient of Na^+ (D^J_{Na}) at 300 K was estimated to be 2.5×10^{-11} cm^2/s with a thermal activation energy of 39(7) meV.

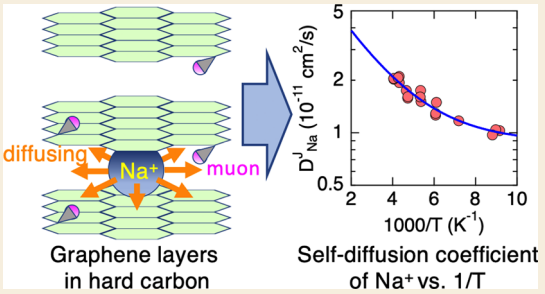

KEYWORDS: *Na-ion battery, hard carbon, anode, ion diffusion, muon spin rotation and relaxation*

INTRODUCTION

Recently, Na-ion battery materials have attracted considerable attention[1−3] because sodium is more abundant than lithium, resulting in lower material costs. Na has a relative abundance of 2.83%, whereas Li has only 0.0065%.[4] Although several Na transition-metal oxides are available as a cathode material for Na-ion batteries, the most common anode materials for Li-ion batteries, that is, graphite and soft carbon, are not compatible with Na-ion batteries. This is because graphite is electrochemically inactive in an insertion and extraction reaction of Na^+-ions.

Conversely, because nongraphitizable carbon, that is, "hard carbon", is electrochemically active as a Na insertion host,[5] hard carbon has been heavily investigated as an anode material for Na-ion batteries.[6−8] Further, hard carbon comprises mainly two structural regions: one is a region of randomly oriented graphene layers, and the other is a region of nanosized voids, that is, a micropore region. However, the relationship between the structure of hard carbon and dynamics of the inserted Na^+ is still not fully understood despite the studies over the past decade. Particularly, a reliable self-diffusion coefficient of Na^+ (D^J_{Na}) has not been reported for Na-inserted hard carbon, although it is an intrinsic physical constant to represent Na^+ dynamics in materials.

Instead, electrochemical techniques have been used to determine the chemical diffusion coefficient (D^C), which is defined by the Fick law under a Na^+ concentration gradient, using a half-cell[9−11] that comprises an electrode of a target material, Na metal as a counter electrode, and electrolyte. Notably, to estimate D^C from the obtained electrochemical data, we definitely need a correct reaction area (A_{re}) of the target material in the half-cell because the time evolution of the current $[I(t)]$ of the half-cell is proportional to $\sqrt{D^C}A_{re}\frac{1}{\sqrt{t}}$ according to the Cottrell equation.[12] However, it is challenging, and eventually impossible, to determine the correct A_{re} in a liquid or solid electrolyte. Thus, D^C is usually estimated using the electrode geometrical area, resulting in an apparent D^C ($D^{C,app}$). Consequently, $D^{C,app}$ is no longer an intrinsic physical constant, but a quantity depending on the fabrication process of the electrode and a combination of the electrode and electrolyte. Here, D^C is connected with D^J as[13−15]

$$D^C = \Theta D^J \quad (1)$$

Received: October 8, 2021
Revised: November 2, 2021
Accepted: November 3, 2021
Published: November 15, 2021

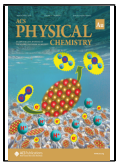

https://doi.org/10.1021/acsphyschemau.1c00036
ACS Phys. Chem Au 2022, 2, 98–107

where Θ denotes a thermodynamic factor independent of A_{re}; therefore, if we use $D^{C,app}$ instead of D^{C} in eq 1, the obtained D^{J} is naturally an apparent D^{J} ($D^{J,app}$), which is also a meaningless parameter for comparing the ion dynamics of one material with that of another material.

The fundamental mechanism of D^{J}_{Na} is based on a thermally activated fluctuation of Na^{+} ions. Thus, in principle, Na nuclear magnetic resonance (NMR) can provide information on such fluctuations. Nevertheless, previous Na-NMR works on Na-inserted hard carbon have reported the resonance line shape but have not provided D^{J}_{Na},[16−18] perhaps due to the difficulty in measuring the spin−lattice relaxation rate ($1/T_1$) in a complex structure of hard carbon. We have therefore attempted to measure the field fluctuation rate in the Na-inserted hard carbon with a positive muon spin rotation and relaxation (μ^{+}SR) technique.

Historically, μ^{+}SR provided reasonable D^{J}_{Li} for Li_xCoO_2 in 2009.[19] Since then, ion dynamics in various battery materials have been successfully studied with μ^{+}SR,[20−33] including Na_xCoO_2,[34] Na_xFePO_4,[35] and C_6Li and $C_{12}Li$.[36] Particularly, in graphite and graphene, an early μ^{+}SR study revealed that the implanted μ^{+} forms a CH-like stable bond[37,38] and the existence of such a bond was supported with recent first-principles calculations.[36] Owing to Li diffusion, the μ^{+} spin in C_6Li experiences a fluctuating nuclear magnetic field from a fixed viewpoint. The obtained D^{J}_{Li} with μ^{+}SR is consistent with D^{J}_{Li} estimated with Li-NMR.[39] Therefore, it is a natural extension to measure D^{J}_{Na} in hard carbon with μ^{+}SR because such a stable CH-like bond is also expected to be formed in Na-inserted hard carbon. Of note, the first μ^{+}SR study on Na-inserted hard carbon has been recently reported by Jensen et al.[40] However, because the μ^{+}SR spectra were measured only in a transverse magnetic field (TF), separating the spin−spin relaxation rate ($1/T_2$) from $1/T_1$ was difficult. Herein, both $1/T_2$ and $1/T_1$ are clearly estimated from the μ^{+}SR data obtained in TF, zero magnetic field (ZF), and longitudinal magnetic field (LF). Here, TF and LF denote the externally applied magnetic field perpendicular and parallel to the initial muon spin polarization, respectively.

RESULTS

TF-μ^{+}SR Measurements

Figure 1 shows the two TF-μ^{+}SR spectra for the C_xNa sample with a state of charge (SOC) of 75% recorded at 50 and 350 K to estimate the temperature variation of a nuclear magnetic field in C_xNa. Because the initial asymmetry (A_0) at time = 0 (t_0) is almost a full value of this setup for both spectra, the all-implanted μ^{+}s are found in a μ^{+} state, indicating the absence of a muonium ($\mu^{+}e^{-}$) state. This is consistent with the metallic

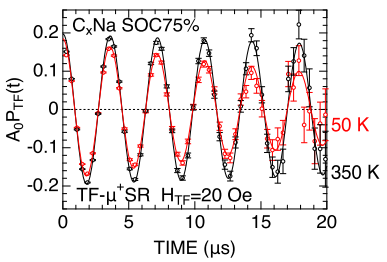

Figure 1. TF-μ^{+}SR spectra for the C_xNa sample with the SOC of 75% recorded at 50 and 350 K. Solid lines represent the best fit using eq 2.

nature of Na-inserted hard carbon. Although the oscillation amplitude caused by TF is clearly damped with time at 50 K, such oscillation is almost time-independent at 350 K, being reproducible to the previous μ^{+}SR study.[40] This implies the dynamic nature of a nuclear magnetic field at 350 K. As a first approximation, the TF-μ^{+}SR spectra were fitted with the exponentially relaxing cosine oscillation

$$A_0 P_{TF} = A_{TF} \cos(2\pi f_{TF} t + \phi_{TF}) \exp(-\lambda_{TF} t) \quad (2)$$

where A_0 denotes the initial asymmetry determined by the TF measurements at high temperatures and P_{TF} represents the muon spin polarization function in TF. A_{TF}, f_{TF}, ϕ_{TF}, and λ_{TF} denote the asymmetry, muon spin precession frequency, initial phase, and relaxation rate due to the applied TF, respectively. Here, $f_{TF} = \gamma_\mu/2\pi \times 20$ Oe = 13.5534 kHz/Oe × 20 Oe ∼ 0.27 MHz, and γ_μ denotes the muon gyromagnetic ratio.

Figure 2 shows the temperature dependence of λ_{TF} for the three C_xNa samples. As the temperature increases from 50 K,

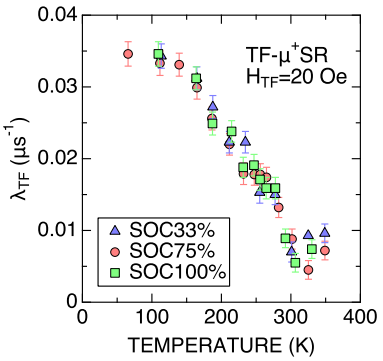

Figure 2. Temperature dependence of the exponential relaxation rate of the TF-μ^{+}SR precession asymmetry for the three C_xNa samples with SOC = 33, 75, and 100%. The data were obtained by fitting the TF-μ^{+}SR spectrum with eq 2.

λ_{TF} of each sample is almost temperature-independent up to 150 K, starts to decrease with increasing temperature, and finally levels off to a very small constant value (about 0.007 μs^{-1}) above approximately 300 K. More precisely, the slope of the $\lambda_{TF}(T)$ curve ($d\lambda_{TF}/dT$) above 250 K is steeper than that below 250 K, which will be discussed later. Because λ_{TF} depends on a spin−spin relaxation rate ($1/T_2$), the observed $\lambda_{TF}(T)$ curves indicate a motional narrowing behavior between 100 and 300 K owing to the dynamics of Na^{+} ions in hard carbon. Noteworthily, regardless of SOC, all the three samples exhibit similar dynamic behavior. Thus, in order to better understand the dynamic behavior in C_xNa, the ZF- and LF-μ^{+}SR spectra were measured and analyzed.

ZF- and LF-μ^{+}SR Measurements

Figure 3 shows the ZF- and two LF-μ^{+}SR spectra recorded at 100, 200, and 300 K. Overall, the μ^{+}SR spectrum exhibits a distinct transition from a low-temperature static to a high-temperature dynamic behavior as the temperature increases. This is consistent with the TF-μ^{+}SR result. However, the ZF-spectra at 100 and 200 K are not explained using the simple dynamic Kubo-Toyabe (G^{DGKT}) function.[41] Therefore, the μ^{+}SR spectra were fitted with a combination of two G^{DGKT} signals from the Na-inserted hard carbon and a time-independent background signal from the Ti sample holder, a Na-free region in hard carbon, and the other materials in the hard carbon electrode

https://doi.org/10.1021/acsphyschemau.1c00036
ACS Phys. Chem Au 2022, 2, 98−107

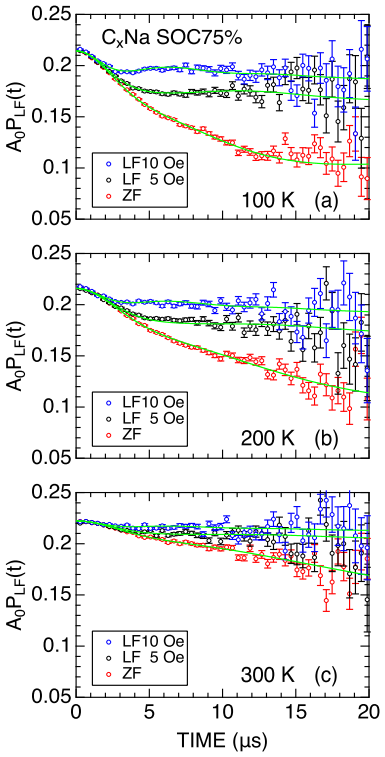

Figure 3. Temperature variation in the ZF- and two LF-μ^+SR spectra recorded at (a) 100, (b) 200, and (c) 300 K. The applied LFs were 5 and 10 Oe. Green solid lines represent the best fit using eq 3.

$$A_0P_{LF}(t) = A_{KT1}G^{DGKT}(t, \Delta_1, \nu_1, H_{LF}) + A_{KT2}G^{DGKT}(t, \Delta_2, \nu_2, H_{LF}) + A_{BG} \quad (3)$$

where P_{LF} denotes the muon spin polarization function in ZF and LF. A_{KT1}, A_{KT2}, and A_{BG} represent asymmetries of the three signals, Δ_1 and Δ_2 denote the field distribution widths, and ν_1 and ν_2 represent the field fluctuation rates of the two G^{DGKT} signals. Here, Δ roughly corresponds to the spin−spin relaxation rate $(1/T_2)$, and ν roughly corresponds to the spin−lattice relaxation rate $(1/T_1)$. For $\nu = 0$ and $H_{LF} = 0$ (i.e., ZF), $G^{DGKT}(t,\Delta,\nu,H_{LF})$ becomes a static Gaussian Kubo−Toyabe function (G_{zz}^{KT}) given as[42]

$$G_{zz}^{KT}(t, \Delta) = \frac{1}{3} + \frac{2}{3}(1 - \Delta^2t^2)\exp\left(-\frac{1}{2}\Delta^2t^2\right) \quad (4)$$

which represents the time variation of the muon spin polarization due to the internal magnetic field formed by randomly oriented static nuclear dipoles with a Gaussian distribution.

The fact that two G^{DGKT} signals are required to fit the μ^+SR spectra suggests that there are two different muon sites in the C_xNa sample with SOC = 75%. A preliminary fit showed that the temperature dependence of Δ_1 is similar to that of Δ_2, and the magnitude of Δ_1 is approximately one-third of that of Δ_2. Combined with the TF-μ^+SR result shown in Figure 2, the implanted muons are most likely to locate in the randomly oriented graphene layers, that is, the graphene layers in C_xNa are assumed as an alternating stack of Na^+-inserted and Na^+-vacant layers, as in the case for $C_{12}Li$. One muon site responsible for the A_{KT2} signal (μ_2 site) is in the Na^+-inserted graphene layer, whereas the other site responsible for the A_{KT1} signal (μ_1 site) is in the Na-vacant graphene layer, as $\Delta_2 > \Delta_1$ (see Figure 6). In other words, the muons at the two sites *see* the Na-diffusion in the graphene layers regardless of the muon sites, being similar to the case for $C_{12}Li$.[36]

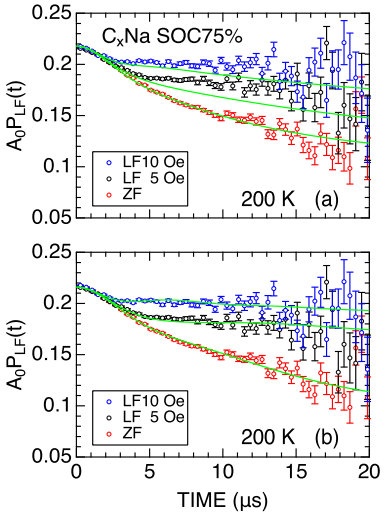

Figure 4. ZF- and two LF-μ^+SR spectra for the C_xNa sample with SOC = 75% recorded at 200 K. In (a), green solid lines represent the best fit using eq 5 with Δ_1 and Δ_2 estimated from the data recorded at 50 K, that is, Δ_1 and Δ_2 are temperature-independent. In (b), green solid lines represent the best fit using eq 3, which are the same as those in Figure 3b.

Because the occupancy of each muon site is independent of temperature, we fitted the ZF- and LF-μ^+SR spectra using common A_{KT1}, A_{KT2}, and A_{BG} in the whole temperature range measured and a common ν for both A_{KT1} and A_{KT2} signals (i.e., $\nu_1 = \nu_2$) at each temperature. The TF-μ^+SR spectrum was also simultaneously fitted using Δ_1, Δ_2, and ν with the Abragam equation (G^A)[28,43,44]

$$A_0P_{TF}(t) = A_{KT,TF}\cos(2\pi f_{TF}t + \phi_{TF})G^A(t) + A_{BG,TF}\cos(2\pi f_{TF}t + \phi_{TF}),$$

$$G^A(t) = \exp\left[-2\frac{\Delta_{av}^2}{\nu^2}(e^{-t\nu} - 1 + t\nu)\right],$$

$$\Delta_{av} = \frac{A_{KT1}\Delta_1 + A_{KT2}\Delta_2}{A_{KT1} + A_{KT2}} \quad (5)$$

Such a combined fit between the Abragam function for the TF-μ^+SR spectrum and the dynamic Kubo-Toyabe function for the ZF- and LF-μ^+SR spectra naturally provides more reliable μ^+SR parameters than the work based only on TF-μ^+SR measurements,[40] where Δ is fixed at Δ(50 K) in the whole measured temperature range, that is, Δ is independent of temperature. In fact, we also attempted to fit the ZF- and LF-μ^+SR spectra using eq 5 with fixed Δ_1 and Δ_2 estimated from the data at 50 K. Such a fit cannot reproduce the two LF spectra even at 200 K, although the fitted ZF spectrum is likely acceptable [see Figure 4a and compare with Figure 4b]. This demonstrates the importance of ZF- and LF-μ^+SR measurements to study ion dynamics in solids and clearly excludes the scenario that both Δ_1 and Δ_2 are independent of temperature in C_xNa.

https://doi.org/10.1021/acsphyschemau.1c00036
ACS Phys. Chem Au 2022, 2, 98−107

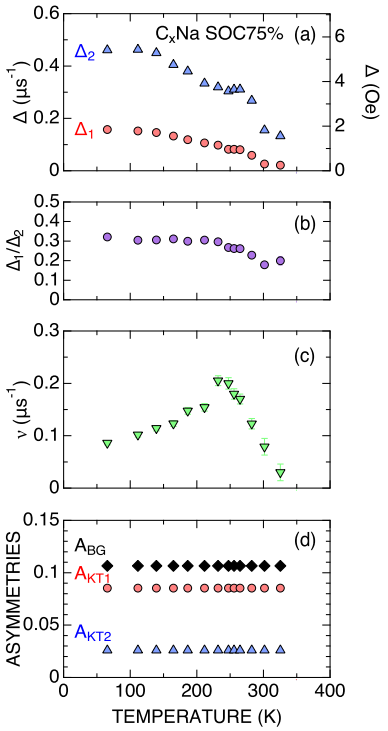

Figure 5. Temperature dependencies of the μ^+SR parameters for C$_x$Na with SOC = 75%: (a) two field distribution widths (Δ_1 and Δ_2), (b) ratio between Δ_1 and Δ_2, (c) common field fluctuation rate (ν) for the two signals, and (d) three asymmetries (A_{KT1}, A_{KT2}, and A_{BG}). The data were obtained by fitting the TF-, ZF- and LF-μ^+SR spectra with eqs 5 and 3. In (a,b,d), error bars are smaller than the symbols. Note that Δ roughly corresponds to a spin−spin relaxation rate ($1/T_2$), whereas ν roughly corresponds to a spin−lattice relaxation rate ($1/T_1$).

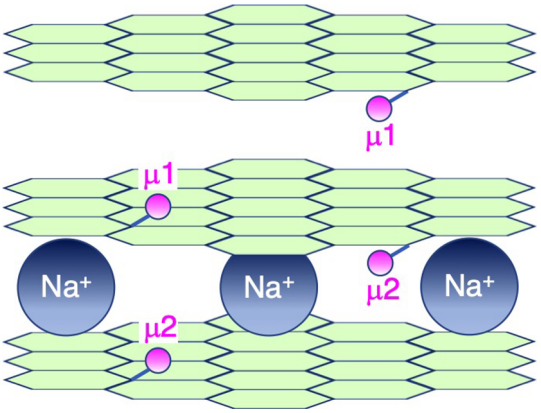

Figure 6. Schematic view of the two muon sites in the Na-inserted graphene layers.

Figure 5 shows the temperature dependencies of the obtained μ^+SR parameters by fitting the TF-, ZF-, and LF-μ^+SR spectra using eqs 3 and 5 for the C$_x$Na sample with SOC = 75%. As temperature increases from 70 K, both Δ_1 and Δ_2 are almost temperature-independent up to about 150 K; then, they start to decrease upon further increasing the temperature, while there is a shoulder in each $\Delta_i(T)$ curve at temperatures between 250 and 270 K. The ratio between Δ_1 and Δ_2 is almost temperature-independent below 250 K, which supports our consideration that both Δ_1 and Δ_2 are caused by a nuclear magnetic field of the Na-inserted graphene layer but *seen* from different viewpoints. At temperatures between 250 and 300 K, the ratio slowly decreases with increasing temperature and then the ratio increases upon further increasing the temperature because Δ_1 is already very small and almost temperature-independent above 300 K.

The μ^+SR result of $C_{12}Li$ (see Figure 7)[36] reveals that as the temperature increases from 50 K, both Δ_1 and Δ_2 are roughly

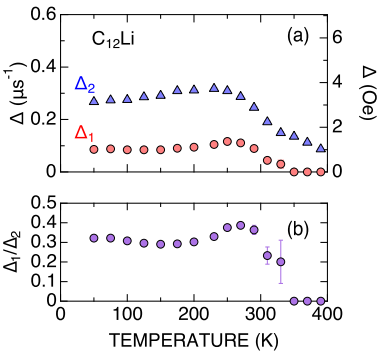

Figure 7. Temperature dependencies of (a) Δ_1 and Δ_2 and (b) Δ_1/Δ_2 for $C_{12}Li$ (reproduced from ref 36. with permission from the PCCP Owner Societies.)

temperature-independent up to about 250 K, then decrease upon further increasing the temperature up to about 350 K, and finally level off to a constant value ($\Delta_1 = 0$). The decreases in Δ_1 and Δ_2 naturally correspond to the motional narrowing behavior due to Li diffusion. Making comparison with the present result on C$_x$Na with SOC = 75%, the inserted Na^+ ions are found to start to diffuse above around 150 K because of the gradual decreases in Δ_1 and Δ_2 above 150 K. The temperature width of the motional narrowing behavior is about 100 K (from 250 to 350 K) for $C_{12}Li$, whereas it is about 150 K (from 150 to 300 K) for C$_x$Na with SOC = 75%. This implies that inhomogeneous local structural environments of hard carbon lead to Na diffusion even at low temperatures.

Evidently, ν increases with increasing temperature up to around 250 K, but it decreases upon further increasing the temperature. The obtained three asymmetries are estimated as $A_{KT1} = 0.0853(6)$, $A_{KT2} = 0.0259(5)$, and $A_{BG} = 0.1066(8)$. Therefore, because the A_{KT1} signal has a predominant contribution to ν, the $\nu(T)$ curve exhibits a local maximum when $\nu > \Delta_1$. Overall, a diffusive behavior is observed in the Na-inserted graphene layer with ZF- and LF-μ^+SR. However, it is ambiguous whether the information on Na diffusion is obtained for the defects, that is, the nanosized void region of hard carbon.

Figures 8 and 9 show the TF-, ZF-, and LF-μ^+SR results for the remaining two C$_x$Na samples with SOC = 33% and 100%. Each μ^+SR parameter shows a temperature dependence similar to that of the C$_x$Na sample with SOC = 75%, as expected from the TF-μ^+SR measurement. The detailed change of the μ^+SR parameters with SOC and the extraction of D^J_{Na} from the $\nu(T)$ curve is discussed in the next section.

DISCUSSION

Which Parameter Changes with the SOC?

With increasing SOC, the amount of Na^+ ions inserted into hard carbon increases linearly. Therefore, the corresponding μ^+SR parameters are also expected to show a monotonic change with the SOC.

https://doi.org/10.1021/acsphyschemau.1c00036
ACS Phys. Chem Au 2022, 2, 98−107

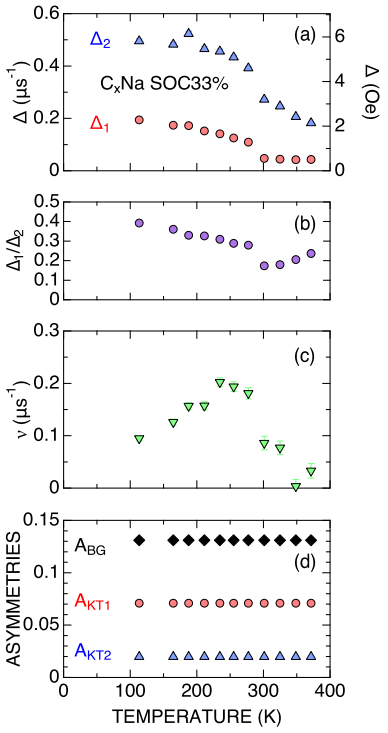

Figure 8. Temperature dependencies of the μ^+SR parameters for C_xNa with SOC = 33%: (a) Δ_1 and Δ_2, (b) Δ_1/Δ_2, (c) ν, and (d) A_{KT1}, A_{KT2}, and A_{BG}.

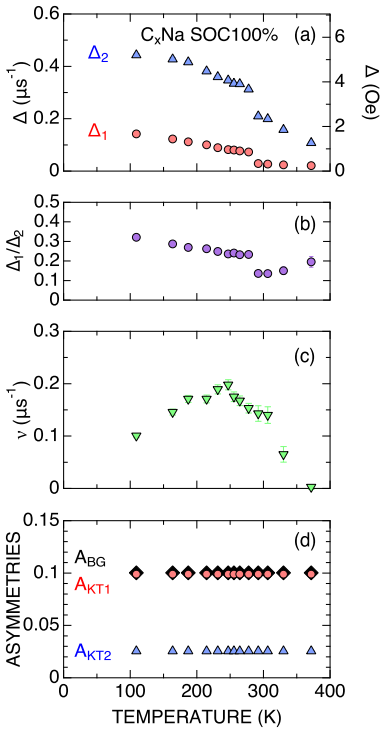

Figure 9. Temperature dependencies of the μ^+SR parameters for C_xNa with SOC = 100%: (a) Δ_1 and Δ_2, (b) Δ_1/Δ_2, (c) ν, and (d) A_{KT1}, A_{KT2}, and A_{BG}.

Figure 10 shows the relationship between four μ^+SR parameters and the SOC in the C_xNa samples; that is, Δ_1, Δ_2, and Δ_1/Δ_2 at 100 K, their asymmetries, and A_{KT1}/A_{KT2}. In addition, the data for $C_{12}Li$ are plotted for comparison. Both

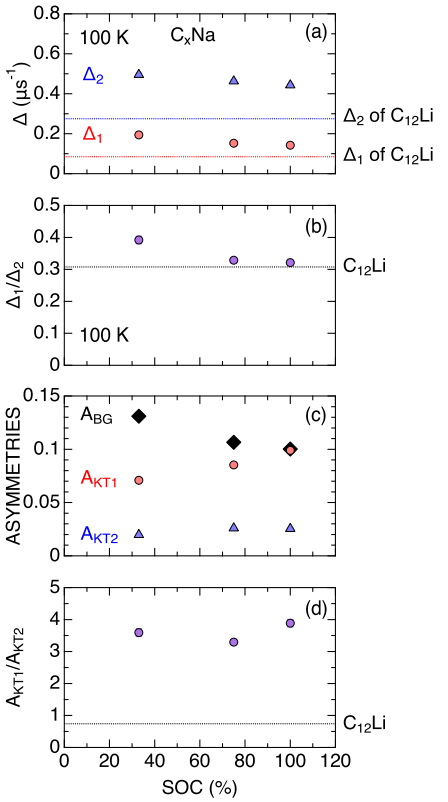

Figure 10. Relationship between the μ^+SR parameters and SOC for C_xNa: (a) Δ_1 and Δ_2 at 100 K, (b) Δ_1/Δ_2 at 100 K, (c) A_{KT1}, A_{KT2}, and A_{BG}, and (d) A_{KT1}/A_{KT2}. Broken lines represent the data for $C_{12}Li$ at 100 K.[36]

Δ_1 and Δ_2 are roughly independent of the SOC, which is also confirmed by the relationship between Δ_1/Δ_2 and the SOC. Furthermore, because Δ_1/Δ_2 for C_xNa is close to that for $C_{12}Li$, the site assignment for the A_{KT1} and A_{KT2} signals is reasonable. The temperature dependence of Δ_1/Δ_2 for $C_{12}Li$[36] [see Figure 7b] is similar to that for the C_xNa samples [Figures. 5b, 8b, and 9b]. Moreover, the fact that both Δ_1 and Δ_2 for C_xNa are larger than those for $C_{12}Li$ suggests that the distance between μ^+ and the nearest neighboring Na^+ in C_xNa is shorter than that between μ^+ and Li^+ in $C_{12}Li$, perhaps due to the distortion of the graphene layers in hard carbon.

As seen in Figure 6, A_{KT2} is thought to be directly correlated with the Na content in the graphene layers because the μ_2 site is closer to the Na^+ ion in the graphene layer than the μ_1 site. In fact, as the SOC increases from 0 to 75%, A_{KT2} increases with the SOC, whereas A_{KT2} levels off to a constant value at SOC > 75%, being consistent with the commonly accepted insertion mechanism,[7] that is, Na^+ ions are inserted into the graphene region at low SOCs and then inserted into the nanosized void region at high SOCs. Since $A_{KT1}/A_{KT2} \sim 3.6$ is almost independent of the SOC, the increase in A_{KT1} is explained by the change in A_{KT2}. This also implies that the μ_1 site is more preferable for the implanted μ^+s than the μ_2 site, probably because of the electrostatic repulsion between Na^+ and μ^+. Furthermore, because A_{KT1}/A_{KT2} for C_xNa (~3.6) is very large compared with that for $C_{12}Li$ (0.74), the Na composition of the graphene layers, that is, the C/Na ratio should be less than 12.

Instead, as the SOC increases, A_{BG} decreases, indicating a decrease in the Na-free region in the graphene layers.

https://doi.org/10.1021/acsphyschemau.1c00036
ACS Phys. Chem Au 2022, 2, 98−107

Conversely, there is no information on the Na dynamics in the nanosized void region in C_xNa with μ^+SR, most likely because of the electrostatic repulsion between the implanted μ^+ and Na^+ in the voids. In other words, the implanted μ^+ values are mostly found in the graphene layers and the amount of the μ^+ sitting in the voids is negligibly small in comparison to the μ^+SR sensitivity, that is, less than 5%.

Self-Diffusion Coefficient

Finally, we attempt to estimate a self-diffusion coefficient of Na^+ in C_xNa (D^J_{Na}) from the present μ^+SR result. Assuming that the position and jump pathway of Na^+ in the graphene layers are the same as those for $C_{12}Li$ and ν corresponds to the hopping rate of Na^+, D^J_{Na} is given by a random walk model in the graphene layers[45]

$$D^J_{Na} = \sum_{i=1}^{n} \frac{1}{N_i} Z_{v,i} s_i^2 \nu \quad (6)$$

where N_i denotes the number of Na sites in the ith jump path, $Z_{v,i}$ represents the vacancy fraction, and s_i denotes the jump distance. Using the data for $C_{12}Li$, $n = 1$, $N_1 = 6$, $Z_1 = 1$, and $s_1 = 0.248$ nm.

Figure 11 shows the relationship between ν and inverse temperature for the three C_xNa samples. Because D^J_{Na} is

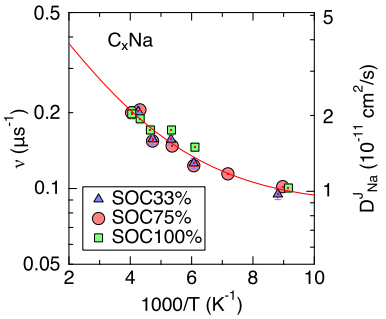

Figure 11. Relationship between ν and inverse temperature for the three C_xNa samples. The right axis shows the corresponding self-diffusion coefficient of Na^+ (D^J_{Na}). A solid line represents the best fit using a thermal activation process with $\nu = \nu_0 + \nu_1 \exp(-E_a/T)$ at temperatures below 250 K, where E_a is an activation energy and is estimated as $E_a = 39(7)$ meV.

proportional to ν in eq 6, the right vertical axis of Figure 11 is converted to D^J_{Na}. The thermal activation energy (E_a) for Na diffusion was estimated as 39(7) meV, which is about half of E_a reported by the recent TF-μ^+SR paper [88(13) meV].[40] This is because, in such a paper, ν was estimated only from the TF-μ^+SR spectrum using eq 5 with a temperature-independent Δ obtained at 50 K.

In comparison with the result of $C_{12}Li$, E_a for the Na diffusion in C_xNa is approximately one-fourth of the E_a for Li diffusion in $C_{12}Li$ [170(20) meV].[36] This indicates the effect of the interlayer distance of the graphene layers on ion diffusion. The c-axis length of graphite for $C_{12}Li$ is 0.335 nm, whereas that of hard carbon is approximately 0.4 nm. Such an elongation of the interlayer distance enables the Na insertion reaction and reduces the energy barrier of ion diffusion. From the solid line in Figure 11, the magnitude of D^J_{Na} is estimated as 2.5×10^{-11} cm^2/s at 300 K and 2.6×10^{-11} cm^2/s at 310 K, whereas $D^J_{Li} = 14.6(4) \times 10^{-11}$ cm^2/s in $C_{12}Li$ at 310 K and $7.6(3) \times 10^{-11}$ cm^2/s in C_6Li at 310 K.

As mentioned in the Introduction, D^J_{Na} estimated with Na-NMR is unavailable at present. This implies that there are no reliable experimental data to compare with the present μ^+SR result. Therefore, we herein compare the μ^+SR results with the predicted D^J_{Na} and D^J_{Li} with MD simulations[46,47] and first-principles calculations,[48,49] combined with D^J_{Li} in C_6Li estimated with Li-NMR[39] (see Table 1). Although the

Table 1. D^J_{Na} and D^J_{Li} Estimated with μ^+SR and Predicted with Molecular Dynamics (MD) Simulations[46,47] and First-Principles (DFT) Calculations[48,49a]

ion in material	method	D^J (cm^2/s)	temperature (K)	refs
Na^+ in hard carbon	μ^+SR	2.5×10^{-11}	300	present work
Li^+ in graphite ($C_{12}Li$)	μ^+SR	$14.6(4) \times 10^{-11}$	310	36
Li^+ in graphite (C_6Li)	μ^+SR	$7.6(3) \times 10^{-11}$	310	36
Li^+ in graphite (C_6Li)	Li-NMR	10^{-11}	295	39
Na^+ in hard carbon	MD simulations	1.43×10^{-8}	room temperature	46
Li^+ in hard carbon	MD simulations	1.63×10^{-7}	room temperature	46
Li^+ in graphite (C_6Li)	MD simulations	10^{-7} (for D^C_{Li})	room temperature	47
Li^+ in graphite (C_6Li)	DFT calculations	1.0×10^{-10}	room temperature	48, 49

[a]Moreover, D^J_{Li} for C_6Li estimated with Li-NMR[39] is listed for comparison. In refs 48 and 49, $D^J_{Li} = D^C_{Li}$ because $\Theta = 1$.

predicted D^J strongly depends on the calculation methods, D^J_{Li} is larger than D^J_{Na} by 1 order of magnitude or more. Such a relation, that is, $D^J_{Li} > D^J_{Na}$, is also observed in the estimated values with μ^+SR, being qualitatively consistent with the predictions.

As seen in Figures 5, 8, and 9, the diffusive behavior is not clearly seen in the $\nu(T)$ curve at temperatures above 250 K because ν becomes larger than Δ_1, resulting in the decrease in ν with increasing temperature. Conversely, TF-μ^+SR measurements provided a motional narrowing behavior up to approximately 300 K (see Figure 2). Therefore, Figure 12 shows the relationship between $1/\lambda_{TF}$ and inverse temperature

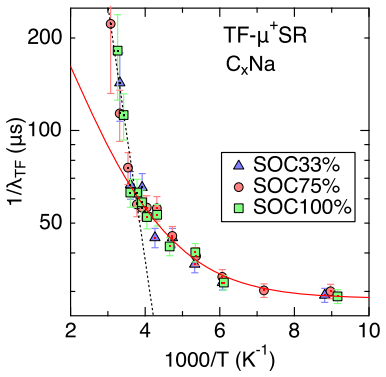

Figure 12. Relationship between $1/\lambda_{TF}$ and inverse temperature for the three C_xNa samples. A solid line represents the best fit using a thermal activation process with $\lambda_{TF}^{-1} = {\lambda_{TF0}}^{-1} + {\lambda_{TF1}}^{-1} \exp(-E_a/T)$ at temperatures below 250 K. E_a is estimated as $E_a = 68(12)$ meV. A similar fit at temperatures above 250 K with ${\lambda_{TF0}}^{-1} = 0$ provides $E_a = 164(16)$ meV, as represented by a dotted line.

https://doi.org/10.1021/acsphyschemau.1c00036
ACS Phys. Chem Au 2022, 2, 98−107

for the three samples. Note that λ_{TF} depends not only on Δ but also on ν, $A_{KT,TF}$, and $A_{BG,TF}$ according to eqs 2 and 5

$$\exp(-\lambda_{TF}t) = \frac{A_{KT,TF}}{A_{TF}} \exp\left[-2\frac{\Delta_{av}^{2}}{\nu^{2}}(e^{-t\nu} - 1 + t\nu)\right] + \frac{A_{BG,TF}}{A_{TF}},$$
$$A_{TF} = A_{KT,TF} + A_{BG,TF} \quad (7)$$

Therefore, λ_{TF} is a complex parameter to show the change in a nuclear magnetic field. When we fitted the $1/\lambda_{TF}(T)$ curve using a thermal activation process at temperatures below 250 K, E_a is estimated as 68(12) meV, which agrees with E_a estimated from the recent TF-μ^+SR work [88(13) meV][40] within the estimation error. However, as the temperature increases from 250 K, $1/\lambda_{TF}$ increases more rapidly than the prediction from a thermally activated process with E_a = 68(12) meV. This implies the presence of another diffusion process with E_a = 164(16) meV, perhaps due to Na diffusion in a nanosized void region, although the detailed information on such diffusion is unlikely to be extractable from the present μ^+SR data.

CONCLUSIONS

We examined the μ^+SR spectra for three C_xNa samples with a different SOC (33, 75, and 100%) in TF, ZF, and LF magnetic fields to determine a self-diffusion coefficient of Na^+ (D_{Na}^{J}) in Na-inserted hard carbon (C_xNa) at temperatures between 50 and 350 K. The TF-μ^+SR measurements showed the appearance of a motional narrowing behavior at temperatures between 150 and 300 K due to Na diffusion. A detailed analysis of the ZF- and LF-μ^+SR spectra showed that there are two muon sites, which were assigned to the graphene layers in C_xNa. Namely, one site is in the Na-inserted graphene layer, whereas the other site is in the Na-vacant graphene layer adjacent to the Na-inserted graphene layer. For both sites, the field fluctuation rate increased with increasing temperature, whereas the filed distribution width decreased with increasing temperature. Furthermore, the above μ^+SR parameters were roughly independent of SOC, indicating that the majority of the implanted muons are located in the graphene layers. Using a random walk model, D_{Na}^{J} in the graphene layer was estimated as 2.5×10^{-11} cm^2/s at 300 K with a thermal activation energy of 39(7) meV. Conversely, the information on Na dynamics in the nanosized void region was not clearly obtained with the present μ^+SR owing to the absence of implanted muons in such a region.

EXPERIMENTAL SECTION

Fabrication of the Test Cell

In order to prepare C_xNa, a Na-ion half-cell was fabricated with hard carbon and Na metal as the electrodes. At first, a hard carbon electrode sheet was prepared by casting slurry, which comprised 85 wt % of hard carbon [Carbotron *P*(*J*), Kureha], 7.5 wt % of acetylene black (Li-400, Denka Company Ltd), 5 wt % of styrene−butadiene rubber (TRD2001, JSR), and 2.5 wt % of sodium carboxymethyl cellulose (CMC#2200, Daicel Miraizu Ltd.), onto a 20 μm thick Ti foil (Hohsen). The resultant composite electrode used in this work was not compressed, and its thickness (excluding the Ti current collector) was ca. 750 μm. Then, the half-cell was assembled in an Ar-filled glovebox by using Na metal as the counter electrode. The electrolyte was 1 M sodium bis(fluorosulfonyl)amide [$Na(FSO_2)_2N$, Solvionic] dissolved in a mixed solution (1/1 v/v) of ethylene carbonate (EC, battery grade, Kishida Chemical) and diethyl carbonate (battery grade, Kishida Chemical). The detailed process has been described elsewhere.[7]

Electrochemical Preparation

The half-cell was charged and discharged at 8.3 mA/g in the voltage (E) range between 0.002 and 2 V under a constant current−constant voltage (cc−cv) condition. For the charging sequence, the potential was kept at 0.002 V for 12 h after constant current charging. The charge and discharge rates (8.3 mA/g) are $C/30$, that is, $1C$ = 250 mA/g. Electrochemical measurements were performed at room temperature (ca. 25 °C) using an electrochemical analyzer (SP-200, Biologic). Figure 13 shows the relationship between potential [E (V vs Na^+/Na)] and specific capacity (mA h/g) for the half-cell at the second cycle, where Na^+ ions are inserted into hard carbon when E decreases, while Na^+ ions are extracted from hard carbon when E increases.

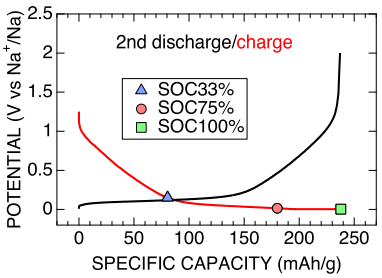

Figure 13. Discharge (Na extraction) and charge (Na insertion) curves in the second cycle for a half-cell comprising hard carbon and Na metal. The three SOC values represent the samples for the present μ^+SR measurements.

The following three samples were prepared: after the initial cycle, the half-cell was charged to E = 0.15 V, which corresponds to a SOC of 33%. SOC was determined based on the discharge capacity obtained at the second cycle, that is, 237 mA h/g is defined as SOC = 100%. For the second sample, the half-cell was further charged up to a specific capacity = 180 mA h/g, which corresponds to the SOC of 75%. After the initial cycle, the fully charged half-cell was kept at 0 V versus Na^+/Na overnight for the preparation of the sample with SOC = 100%. The compositions of the three samples were estimated from the specific capacity to be $C_{20}Na$, $C_{8.9}Na$, and $C_{6.8}Na$ for the samples with SOC = 33, 75, and 100%, respectively, assuming one-electron transfer for the charge and discharge reactions. Note that three half-cells were prepared for each condition to get the enough amount of the active materials for μ^+SR measurements. Each half-cell was disassembled after second charging as the passivation films could be formed during the first charging reaction which avoids self-discharge during sample preparation in the glovebox.

Positive Muon Spin Rotation and Relaxation

Immediately before the μ^+SR experiment, the C_xNa sheets were removed from the half-cells and then dried in a He-filled glovebox for a few minutes. The electrode was then peeled off from the Ti foil. Approximately 800 mg of the electrode was packed into a gold O-ring sealed titanium (Ti) cell (see Figure 14) because C_xNa is very sensitive to moisture in air. The sample space of the Ti cell is 24 mm in diameter and 1 mm in depth. Because the range of the surface muons is 150−200 mg/cm^2, the muons easily penetrate a Ti window with 50 μm thickness corresponding to ~23 mg/cm^2 but stop into the electrode with approximately 177 mg/cm^2[= 800/(π1.2^2)].

The μ^+SR experiments were performed on the **S1** surface muon beamline at the MUSE MLF of J-PARC in Japan. In order to know a small change in an internal nuclear magnetic field due to Na diffusion, the μ^+SR spectra were recorded in a ZF, LF, and TF in the temperature (T) range between 50 and 375 K using a microstat

https://doi.org/10.1021/acsphyschemau.1c00036
ACS Phys. Chem Au 2022, 2, 98−107

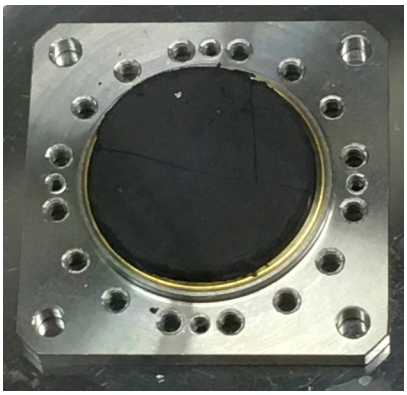

Figure 14. Titanium cell filled with the C_xNa electrode (black color) together with a gold O-ring for sealing. The size of the sample space is 24 mm diameter and 1 mm depth.

(Oxford). Here, the LF and TF denote the externally applied magnetic field parallel and perpendicular to the initial muon spin polarization, respectively. The sample in the Ti-cell was mounted on the Cu holder of the microstat, which was cooled down to 10 K using a liquid He flow and heated up to around 400 K without a setup change. The details of the experimental technique have been described elsewhere.[19,34,36,50,51] The obtained μ^+SR data were analyzed using musrfit.[52]

AUTHOR INFORMATION

Corresponding Authors

Kazuki Ohishi − *Neutron Science and Technology Center, Comprehensive Research Organization for Science and Society (CROSS), Ibaraki 319-1106, Japan*; Email: k_ohishi@cross.or.jp

Jun Sugiyama − *Neutron Science and Technology Center, Comprehensive Research Organization for Science and Society (CROSS), Ibaraki 319-1106, Japan; Advanced Science Research Center, Japan Atomic Energy Agency, Ibaraki 319-1195, Japan*; orcid.org/0000-0002-0916-5333; Phone: +81 (0)29-219-5300; Email: juns@triumf.ca, j_sugiyama@cross.or.jp

Authors

Daisuke Igarashi − *Department of Applied Chemistry, Tokyo University of Science, Tokyo 162-8601, Japan*

Ryoichi Tatara − *Department of Applied Chemistry, Tokyo University of Science, Tokyo 162-8601, Japan; Elements Strategy Initiative for Catalysts and Batteries (ESICB), Kyoto University, Kyoto 615-8245, Japan*; orcid.org/0000-0002-8148-5294

Shoichiro Nishimura − *Muon Science Laboratory, Institute of Materials Structure Science, KEK, Ibaraki 319-1106, Japan*

Akihiro Koda − *Muon Science Laboratory, Institute of Materials Structure Science, KEK, Ibaraki 319-1106, Japan*

Shinichi Komaba − *Department of Applied Chemistry, Tokyo University of Science, Tokyo 162-8601, Japan; Elements Strategy Initiative for Catalysts and Batteries (ESICB), Kyoto University, Kyoto 615-8245, Japan*; orcid.org/0000-0002-9757-5905

Complete contact information is available at: https://pubs.acs.org/10.1021/acsphyschemau.1c00036

Author Contributions

J.S. conceived the experiments with K.O. D.I., R.T., and S.K. prepared the samples, and D.I. and R.T. performed the μ^+SR experiments in J-PARC together with K.O. and J.S. and the local J-PARC support from S.N. and A.K. J.S. analyzed the data and created the first draft with K.O. D.I., R.T., and S.K. edited the draft. All authors reviewed the manuscript in several steps.

Notes

The authors declare no competing financial interest.

ACKNOWLEDGMENTS

We thank the staff of J-PARC (especially the MUSE) for help with the μ^+SR experiments (proposal no. 2020B0252), I. Umegaki for the discussion, and Enago (www.enago.jp) for the English language review. D.I., R.T., and S.K. were partly supported by the MEXT program "ESICB" (JPMXP0112101003). This work was supported by the Japan Society for the Promotion Science (JSPS) KAKENHI grant nos. JP18H01863 and JP20K21149.

REFERENCES

(1) Palomares, V.; Serras, P.; Villaluenga, I.; Hueso, K. B.; Carretero-González, J.; Rojo, T. Na-ion batteries, recent advances and present challenges to become low cost energy storage systems. *Energy Environ. Sci.* **2012**, *5*, 5884−5901.

(2) Yabuuchi, N.; Kubota, K.; Dahbi, M.; Komaba, S. Research Development on Sodium-Ion Batteries. *Chem. Rev.* **2014**, *114*, 11636−11682.

(3) Hwang, J.-Y.; Myung, S.-T.; Sun, Y.-K. Sodium-ion batteries: present and future. *Chem. Soc. Rev.* **2017**, *46*, 3529−3614.

(4) Clarke, F. W. *The Data of Geochemistry*; Government Printing Office: Washington, 1908.

(5) Stevens, D. A.; Dahn, J. R. High Capacity Anode Materials for Rechargeable Sodium-Ion Batteries. *J. Electrochem. Soc.* **2000**, *147*, 1271.

(6) Izanzar, I.; Dahbi, M.; Kiso, M.; Doubaji, S.; Komaba, S.; Saadoune, I. Hard carbons issued from date palm as efficient anode materials for sodium-ion batteries. *Carbon* **2018**, *137*, 165−173.

(7) Kubota, K.; Shimadzu, S.; Yabuuchi, N.; Tominaka, S.; Shiraishi, S.; Abreu-Sepulveda, M.; Manivannan, A.; Gotoh, K.; Fukunishi, M.; Dahbi, M.; Komaba, S. Structural Analysis of Sucrose-Derived Hard Carbon and Correlation with the Electrochemical Properties for Lithium, Sodium, and Potassium Insertion. *Chem. Mater.* **2020**, *32*, 2961−2977.

(8) Xie, F.; Xu, Z.; Guo, Z.; Titirici, M.-M. Hard carbons for sodium-ion batteries and beyond. *Prog. Nucl. Energy* **2020**, *2*, 042002.

(9) Kondo, Y.; Fukutsuka, T.; Miyazaki, K.; Miyahara, Y.; Abe, T. Investigation of Electrochemical Sodium-Ion Intercalation Behavior into Graphite-Based Electrodes. *J. Electrochem. Soc.* **2019**, *166*, A5323−A5327.

(10) Ledwoch, D.; Robinson, J. B.; Gastol, D.; Smith, K.; Shearing, P. R.; Brett, D. J. L.; Kendrick, E. Hard Carbon Composite Electrodes for Sodium-Ion Batteries with Nano-Zeolite and Carbon Black Additives. *Batteries Supercaps* **2021**, *4*, 163−172.

(11) Yang, J.; Wang, X.; Dai, W.; Lian, X.; Cui, X.; Zhang, W.; Zhang, K.; Lin, M.; Zou, R.; Loh, K. P.; Yang, Q.-H.; Chen, W. From Micropores to Ultra-micropores inside Hard Carbon: Toward Enhanced Capacity in Room-/Low-Temperature Sodium-Ion Storage. *Nano-Micro Lett.* **2021**, *13*, 98.

(12) Bard, A. J.; Faulkner, L. R. *Electrochemical Methods: Fundamentals and Applications*, 2nd ed.; Wiley, 2001.

(13) Van der Ven, A.; Ceder, G. Lithium Diffusion in Layered Li_xCoO_2. *Electrochem. Solid-State Lett.* **2000**, *3*, 301−304.

(14) Gomer, R. Diffusion of adsorbates on metal surfaces. *Rep. Prog. Phys.* **1990**, *53*, 917−1002.

(15) Wen, C. J.; Boukamp, B. A.; Huggins, R. A.; Weppner, W. Thermodynamic and Mass Transport Properties of LiAl. *J. Electrochem. Soc.* **1979**, *126*, 2258−2266.
(16) Gotoh, K.; Ishikawa, T.; Shimadzu, S.; Yabuuchi, N.; Komaba, S.; Takeda, K.; Goto, A.; Deguchi, K.; Ohki, S.; Hashi, K.; Shimizu, T.; Ishida, H. NMR study for electrochemically inserted Na in hard carbon electrode of sodium ion battery. *J. Power Sources* **2013**, *225*, 137−140.
(17) Stratford, J. M.; Allan, P. K.; Pecher, O.; Chater, P. A.; Grey, C. P. Mechanistic insights into sodium storage in hard carbon anodes using local structure probes. *Chem. Commun.* **2016**, *52*, 12430−12433.
(18) Bray, J. M.; Doswell, C. L.; Pavlovskaya, G. E.; Chen, L.; Kishore, B.; Au, H.; Alptekin, H.; Kendrick, E.; Titirici, M.-M.; Meersmann, T.; Britton, M. M. Operando visualisation of battery chemistry in a sodium-ion battery by ^{23}Na magnetic resonance imaging. *Nat. Commun.* **2020**, *11*, 2083.
(19) Sugiyama, J.; Mukai, K.; Ikedo, Y.; Nozaki, H.; Månsson, M.; Watanabe, I. Li Diffusion in Li_xCoO_2 Probed by Muon-Spin Spectroscopy. *Phys. Rev. Lett.* **2009**, *103*, 147601.
(20) Sugiyama, J.; Ikedo, Y.; Mukai, K.; Nozaki, H.; Månsson, M.; Ofer, O.; Harada, M.; Kamazawa, K.; Miyake, Y.; Brewer, J. H.; Ansaldo, E. J.; Chow, K. H.; Watanabe, I.; Ohzuku, T. Low-temperature magnetic properties and high-temperature diffusive behavior of $LiNiO_2$ investigated by muon-spin spectroscopy. *Phys. Rev. B: Condens. Matter Mater. Phys.* **2010**, *82*, 224412.
(21) Sugiyama, J.; Nozaki, H.; Harada, M.; Kamazawa, K.; Ofer, O.; Månsson, M.; Brewer, J. H.; Ansaldo, E. J.; Chow, K. H.; Ikedo, Y.; Miyake, Y.; Ohishi, K.; Watanabe, I.; Kobayashi, G.; Kanno, R. Magnetic and diffusive nature of $LiFePO_4$ investigated by muon spin rotation and relaxation. *Phys. Rev. B: Condens. Matter Mater. Phys.* **2011**, *84*, 054430.
(22) Sugiyama, J.; Nozaki, H.; Harada, M.; Kamazawa, K.; Ikedo, Y.; Miyake, Y.; Ofer, O.; Månsson, M.; Ansaldo, E. J.; Chow, K. H.; Kobayashi, G.; Kanno, R. Diffusive behavior in $LiMPO_4$ with M = Fe, Co, Ni probed by muon-spin relaxation. *Phys. Rev. B: Condens. Matter Mater. Phys.* **2012**, *85*, 054111.
(23) Sugiyama, J.; Mukai, K.; Nozaki, H.; Harada, M.; Månsson, M.; Kamazawa, K.; Andreica, D.; Amato, A.; Hillier, A. D. Antiferromagnetic spin structure and lithium ion diffusion in Li_2MnO_3 probed by μ^+SR. *Phys. Rev. B: Condens. Matter Mater. Phys.* **2013**, *87*, 024409.
(24) Sugiyama, J.; Mukai, K.; Harada, M.; Nozaki, H.; Miwa, K.; Shiotsuki, T.; Shindo, Y.; Giblin, S. R.; Lord, J. S. Reactive surface area of $Li_x(Co_{1/3}Ni_{1/3}Mn_{1/3})O_2$ electrode determined by μSR and electrochemical measurements. *Phys. Chem. Chem. Phys.* **2013**, *15*, 10402−10412.
(25) Sugiyama, J.; Nozaki, H.; Umegaki, I.; Mukai, K.; Miwa, K.; Shiraki, S.; Hitosugi, T.; Suter, A.; Prokscha, T.; Salman, Z.; Lord, J. S.; Månsson, M. Li-ion diffusion in $Li_4Ti_5O_{12}$ and $LiTi_2O_4$ battery materials detected by muon spin spectroscopy. *Phys. Rev. B: Condens. Matter Mater. Phys.* **2015**, *92*, 014417.
(26) Sugiyama, J.; Forslund, O. K.; Nocerino, E.; Matsubara, N.; Papadopoulos, K.; Sassa, Y.; Cottrell, S. P.; Hillier, A. D.; Ishida, K.; Månsson, M.; Brewer, J. H. Lithium diffusion in $LiMnPO_4$ detected with $\mu^{\pm}$SR. *Phys. Rev. Res.* **2020**, *2*, 033161.
(27) Matsubara, N.; et al. Magnetism and ion diffusion in honeycomb layered oxide $K_2Ni_2TeO_6$. *Sci. Rep.* **2020**, *10*, 18305.
(28) Sugiyama, J.; Ohishi, K.; Forslund, O. K.; Månsson, M.; Cottrell, S. P.; Hillier, A. D.; Ishida, K. How Li diffusion in spinel $Li[Ni_{1/2}Mn_{3/2}]O_4$ is seen with $\mu^{\pm}$SR. *Z. Phys. Chem.* **2021**, 000010151520213102.
(29) Powell, A. S.; Lord, J. S.; Gregory, D. H.; Titman, J. J. Muon Spin Relaxation Studies of Lithium Nitridometallate Battery Materials: Muon Trapping and Lithium Ion Diffusion. *J. Phys. Chem. C* **2009**, *113*, 20758−20763.
(30) Baker, P. J.; Franke, I.; Pratt, F. L.; Lancaster, T.; Prabhakaran, D.; Hayes, W.; Blundell, S. J. Probing magnetic order in $LiMPO_4$ (M = Ni, Co, Fe) and lithium diffusion in Li_xFePO_4. *Phys. Rev. B: Condens. Matter Mater. Phys.* **2011**, *84*, 174403.
(31) Powell, A. S.; Stoeva, Z.; Lord, J. S.; Smith, R. I.; Gregory, D. H.; Titman, J. J. Insight into lithium transport in lithium nitridometallate battery materials from muon spin relaxation. *Phys. Chem. Chem. Phys.* **2013**, *15*, 816−823.
(32) Johnson, I. D.; Ashton, T. E.; Blagovidova, E.; Smales, G. J.; Lübke, M.; Baker, P. J.; Corr, S. A.; Darr, J. A. Mechanistic insights of Li^+ diffusion within doped $LiFePO_4$ from Muon Spectroscopy. *Sci. Rep.* **2018**, *8*, 4114.
(33) McClelland, I.; Booth, S. G.; El-Shinawi, H.; Johnston, B. I. J.; Clough, J.; Guo, W.; Cussen, E. J.; Baker, P. J.; Corr, S. A. In Situ Diffusion Measurements of a NASICON-Structured All-Solid-State Battery Using Muon Spin Relaxation. *ACS Appl. Energy Mater.* **2021**, *4*, 1527−1536.
(34) Månsson, M.; Sugiyama, J. Muon-spin relaxation study on Li- and Na-diffusion in solids. *Phys. Scr.* **2013**, *88*, 068509.
(35) Sugiyama, J.; Nozaki, H.; Umegaki, I.; Harada, M.; Higuchi, Y.; Ansaldo, E. J.; Brewer, J. H.; Miyake, Y.; Kobayashi, G.; Kanno, R. Structural, magnetic, and diffusive nature of olivine-type Na_xFePO_4. *J. Phys.: Conf. Ser.* **2014**, *551*, 012012.
(36) Umegaki, I.; Kawauchi, S.; Sawada, H.; Nozaki, H.; Higuchi, Y.; Miwa, K.; Kondo, Y.; Månsson, M.; Telling, M.; Coomer, F. C.; Cottrell, S. P.; Sasaki, T.; Kobayashi, T.; Sugiyama, J. Li-ion diffusion in Li intercalated graphite C_6Li and $C_{12}Li$ probed by μ^+SR. *Phys. Chem. Chem. Phys.* **2017**, *19*, 19058−19066.
(37) Chakhalian, J. A.; Kiefl, R. F.; Dunsiger, S. R.; MacFarlane, W. A.; Miller, R.; Sonier, J. E.; Fischer, J. E. Evidence for local moment formation around a positive muon in graphite. *Phys. Rev. B: Condens. Matter Mater. Phys.* **2002**, *66*, 155107.
(38) Riccò, M.; Pontiroli, D.; Mazzani, M.; Choucair, M.; Stride, J. A.; Yazyev, O. V. Muons Probe Strong Hydrogen Interactions with Defective Graphene. *Nano Lett.* **2011**, *11*, 4919−4922.
(39) Langer, J.; Epp, V.; Heitjans, P.; Mautner, F. A.; Wilkening, M. Lithium motion in the anode material LiC_6 as seen via time-domain ^{7}Li NMR. *Phys. Rev. B: Condens. Matter Mater. Phys.* **2013**, *88*, 094304.
(40) Jensen, A. C. S.; Olsson, E.; Au, H.; Alptekin, H.; Yang, Z.; Cottrell, S.; Yokoyama, K.; Cai, Q.; Titirici, M.-M.; Drew, A. J. Local mobility in electrochemically inactive sodium in hard carbon anodes after the first cycle. *J. Mater. Chem. A* **2020**, *8*, 743−749.
(41) Hayano, R. S.; Uemura, Y. J.; Imazato, J.; Nishida, N.; Yamazaki, T.; Kubo, R. Zero-and low-field spin relaxation studied by positive muons. *Phys. Rev. B: Condens. Matter Mater. Phys.* **1979**, *20*, 850−859.
(42) Kubo, R.; Toyabe, T. In*Magnetic Resonance and Relaxation*; Bline, R., Ed.; North-Holland Publishing Company: Amsterdam, 1996; p 810.
(43) Keren, A. Generalization of the Abragam relaxation function to a longitudinal field. *Phys. Rev. B: Condens. Matter Mater. Phys.* **1994**, *50*, 10039−10042.
(44) Abragam, A. *The Principles of Nuclear Magnetism; Reprint with Corrections*; International Series of Monographs on Physics; Clarendon Press: Oxford, 1989.
(45) Borg, R. J.; Dienes, G. J. *An Introduction to Solid State Diffusion*; Academic Press: San Diego, 1988; Chapter 3, pp 53−77.
(46) Kizzire, D. G.; Richter, A. M.; Harper, D. P.; Keffer, D. J. Lithium and Sodium Ion Binding Mechanisms and Diffusion Rates in Lignin-Based Hard Carbon Models. *ACS Omega* **2021**, *6*, 19883−19892.
(47) Persson, K.; Sethuraman, V. A.; Hardwick, L. J.; Hinuma, Y.; Meng, Y. S.; van der Ven, A.; Srinivasan, V.; Kostecki, R.; Ceder, G. Lithium Diffusion in Graphitic Carbon. *J. Phys. Chem. Lett.* **2010**, *1*, 1176−1180.
(48) Toyoura, K.; Koyama, Y.; Kuwabara, A.; Oba, F.; Tanaka, I. First-principles approach to chemical diffusion of lithium atoms in a graphite intercalation compound. *Phys. Rev. B: Condens. Matter Mater. Phys.* **2008**, *78*, 214303.
(49) Toyoura, K.; Koyama, Y.; Kuwabara, A.; Tanaka, I. Effects of Off-Stoichiometry of LiC6 on the Lithium Diffusion Mechanism and

Diffusivity by First Principles Calculations. *J. Phys. Chem. C* **2010**, *114*, 2375−2379.
(50) Kalvius, G. M.; Noakes, D. R.; Hartmann, O. In *Handbook on the Physics and Chemistry of Rare Earths*; Gschneidner, K. A., Eyring, J. L., Lander, G. H., Eds.; Elsevier: North-Holland, Amsterdam, 2001; Vol. *32*; Chapter 206, pp 55−451.
(51) Yaouanc, A.; de Réotier, P. D. *Muon Spin Rotation, Relaxation, and Resonance, Application to Condensed Matter*; Oxford University Press: New York, 2011.
(52) Suter, A.; Wojek, B. M. Musrfit: A Free Platform-Independent Framework for μSR Data Analysis. *Phys. Procedia* **2012**, *30*, 69−73. 12th International Conference on Muon Spin Rotation, Relaxation and Resonance (μSR2011)

https://doi.org/10.1021/acsphyschemau.1c00036
ACS Phys. Chem Au 2022, 2, 98−107